UC San Diego
UC San Diego Previously Published Works

Title

The influence of laser focusing conditions on the direct laser acceleration of electrons

Permalink

https://escholarship.org/uc/item/1m2071mg

Journal

New Journal of Physics, 26(5)

ISSN

1367-2630

Authors

Tang, H
Tangtartharakul, K
Babjak, R
et al.

Publication Date

2024-05-01

DOI

10.1088/1367-2630/ad3be4

Copyright Information

Peer reviewed

PAPER • OPEN ACCESS

The influence of laser focusing conditions on the direct laser acceleration of electrons

To cite this article: H Tang *et al* 2024 *New J. Phys.* **26** 053010

View the article online for updates and enhancements.

New Journal of Physics

The open access journal at the forefront of physics

PAPER

The influence of laser focusing conditions on the direct laser acceleration of electrons

H Tang[1],[*] , K Tangtartharakul[2] , R Babjak[3],[4] , I-L Yeh[5] , F Albert[6], H Chen[6], P T Campbell[1] , Y Ma[1] , P M Nilson[7], B K Russell[1] , J L Shaw[7] , A G R Thomas[1] , M Vranic[3], A V Arefiev[2] and L Willingale[1]

[1] Gérard Mourou Center for Ultrafast Optical Science, University of Michigan, 2200 Bonisteel Boulevard, Ann Arbor, MI 48109, United States of America
[2] Department of Mechanical and Aerospace Engineering, University of California at San Diego, La Jolla, CA 92093, United States of America
[3] GoLP/Instituto de Plasmas e Fusão Nuclear, Instituto Superior Técnico, Universidade de Lisboa, Lisbon 1049-001, Portugal
[4] Institute of Plasma Physics, Czech Academy of Sciences, Za Slovankou 1782/3, 182 00 Praha 8, Czech Republic
[5] Department of Physics, University of California at San Diego, La Jolla, CA 92093, United States of America
[6] Lawrence Livermore National Laboratory, Livermore, CA 94550, United States of America
[7] Laboratory for Laser Energetics, University of Rochester, Rochester, NY 14623, United States of America
[*] Author to whom any correspondence should be addressed.

E-mail: tanghm@umich.edu

Keywords: direct laser acceleration, laser-plasma interaction, electron acceleration

Abstract

Direct laser acceleration of electrons during a high-energy, picosecond laser interaction with an underdense plasma has been demonstrated to be substantially enhanced by controlling the laser focusing geometry. Experiments using the OMEGA EP facility measured electrons accelerated to maximum energies exceeding 120 times the ponderomotive energy under certain laser focusing, pulse energy, and plasma density conditions. Two-dimensional particle-in-cell simulations show that the laser focusing conditions alter the laser field evolution, channel fields generation, and electron oscillation, all of which contribute to the final electron energies. The optimal laser focusing condition occurs when the transverse oscillation amplitude of the accelerated electron in the channel fields matches the laser beam width, resulting in efficient energy gain. Through this observation, a simple model was developed to calculate the optimal laser focal spot size in more general conditions and is validated by experimental data.

1. Introduction

The rapid advancement of ultra-high power laser facilities is enabling the realization of high energy density physics experiments and exploration of next-generation plasma-based accelerators [1, 2]. Direct laser acceleration (DLA) is one of the mechanisms for producing high-flux high-energy electrons [3–5]. DLA has many potential applications in accelerating secondary ions/neutrons/positrons [6–9], providing bright directional x-rays [10], material detection [11] and radiotherapy treatment [12]. For example, ion acceleration can be enhanced when superponderomotive DLA electrons are generated in a laser interaction with a double-layer target [13]. Understanding the energy transfer mechanism from the driving laser pulse to the plasma electrons is essential for these secondary processes.

In DLA process, the accelerated electrons gain energy directly from the laser. Consider a laser pulse with a peak normalized field strength $a_0 = eE_0/(m_e c \omega_0) > 1$, where E_0 is the peak laser electric field amplitude, ω_0 is the laser frequency, c is the speed of light, and e and m_e are the electron charge and mass respectively. The electric field of the laser oscillates the electron in the transverse direction and the $(\mathbf{v} \times \mathbf{B})$ force converts transverse momentum to longitudinal momentum. Previous studies depicted this process in a preformed channel [14]. The channel fields dramatically increase electron energy gain by reducing the negative role of dephasing to keep electrons in phase with laser wave over an extended distance. Previous work has shown that the azimuthal channel magnetic field can confine the electron transverse excursion [15]. Also, in the near critical density regime, the azimuthal channel magnetic field assists electron heating by deflecting

electrons forward, whereas the longitudinal channel electric field directly accelerates the electrons in the forward direction [16]. Simulations performed by Tangtartharakul *et al* show that increasing the focal spot size and matched channel width can further enhance energy coupling efficiency because the negative work done by the longitudinal laser field component is reduced [17]. Counter-intuitively, raising the laser peak intensity by focusing the beam to a smaller spot does not lead to higher electron energy. Babjak *et al* found an analytical prediction for the optimal focal spot, which approximately matches the electron transverse resonant amplitude, for highly relativistic intensity laser pulses over a range of plasma densities [18]. Laser wakefield acceleration is another regime where focusing geometry has been considered an important parameter. A laser with a spot size larger than the plasma wavelength can maintain high intensity and be self-guided in plasma, allowing the acceleration of monoenergetic electron bunches [19]. However, we currently lack direct experimental evidence showing the effect of laser focusing geometries on DLA.
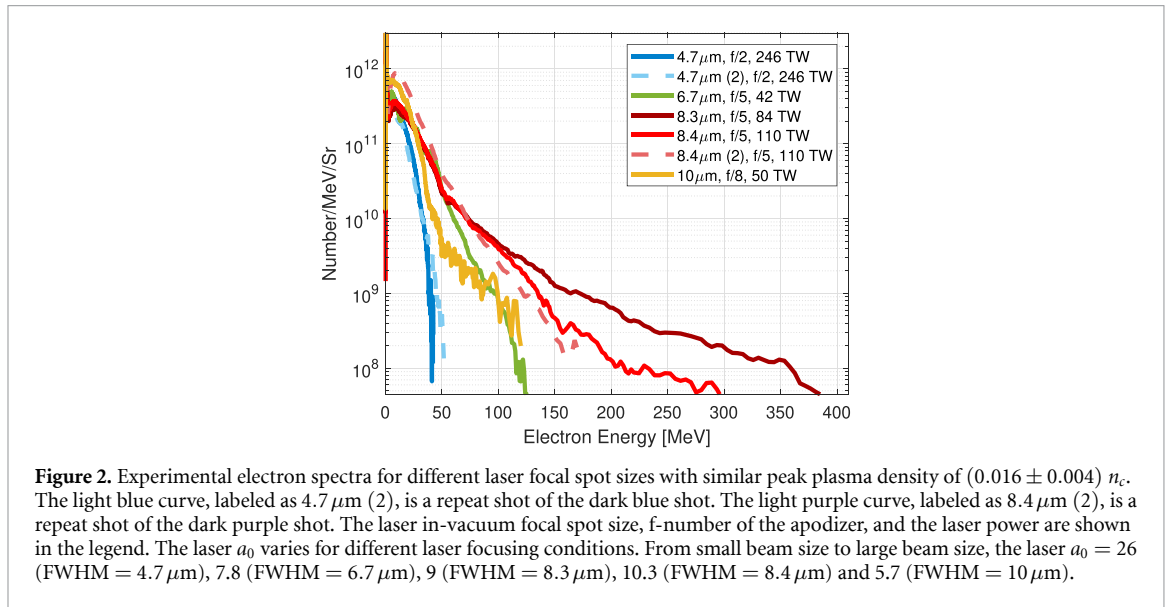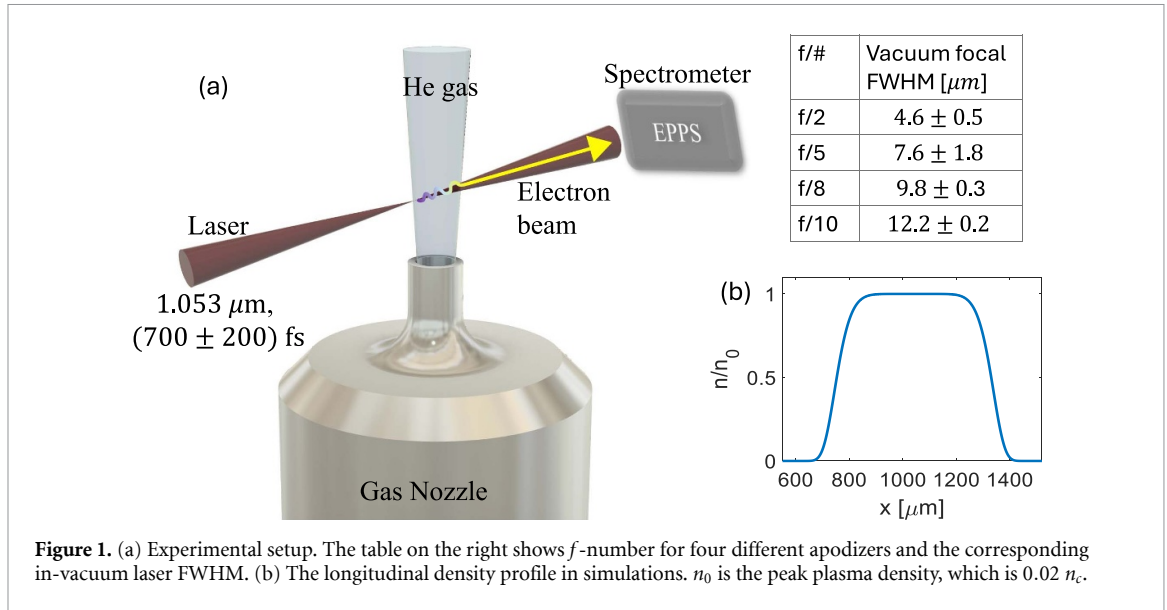
In this paper, the DLA electron energy dependency on laser focusing geometry is investigated using experiments and numerical modeling. The experiments were performed on the OMEGA EP laser facility and demonstrated that the electron energy can be notably changed by varying the laser focal spot size. This observation is strongly supported by complementary 2D particle-in-cell (PIC) OSIRIS simulations [20, 21], which reveal how the evolution of the laser field and the generation of localized fields in plasma affect the accelerated electron motion inside the laser channel. Particle tracking is performed to study the electron trajectories. The relative energy contributions from the laser transverse and longitudinal fields are distinguished, as well as the detrimental effect of the sheath field formed at the rear of the target. The sheath field strength increases with laser beam size, making its effect particularly notable for electrons accelerated by large beams. We find the optimal focusing geometry can be analytically predicted by equating the electron transverse displacement and laser beam width. This method is shown to fit the experimental results over a variety of plasma densities and laser parameters.

2. Experimental setup

The experiment was performed at the University of Rochester Laboratory for Laser Energetics using the OMEGA EP laser facility. Figure 1(a) shows the schematic of the setup. A laser pulse with a central wavelength of $1.053\,\mu$m, duration of (700 ± 200) fs was focused by an $f/2$ equivalent off-axis parabolic mirror to the edge of a Mach $2 - 2$ mm diameter supersonic helium gas jet target. A wide range of peak plasma densities (n_e) from $0.008\,n_c$ to $0.06\,n_c$, where n_c is the critical density, were examined and controlled by adjusting the backing pressure of the He gas. The default near-field beam profile is square. To change the effective f-number of the beam, circular apodizers with different diameters were used so that the full-width at half-maximum (FWHM) focal spot size in vacuum varied from $(4.6 \pm 0.5)\,\mu$m to $(12.2 \pm 0.2)\,\mu$m. The on-shot wavefront was measured and the vacuum focal plane was reconstructed. However, the increase of the beam size led to a reduction of the maximum possible on-target energy, hence limiting the obtainable a_0 for large focal spots. The range of peak vacuum intensities was $(0.15—9.0) \times 10^{20}\,\mathrm{Wcm}^{-2}$, corresponding to an a_0 range of 3.4–27. The electron energy distributions were measured along the laser axis using a magnetic electron–positron-proton particle spectrometer (EPPS) [22] with an energy coverage from 1–150 MeV and the energy uncertainty range from 2% at low energy end to up to 30% at the high energy end [23].
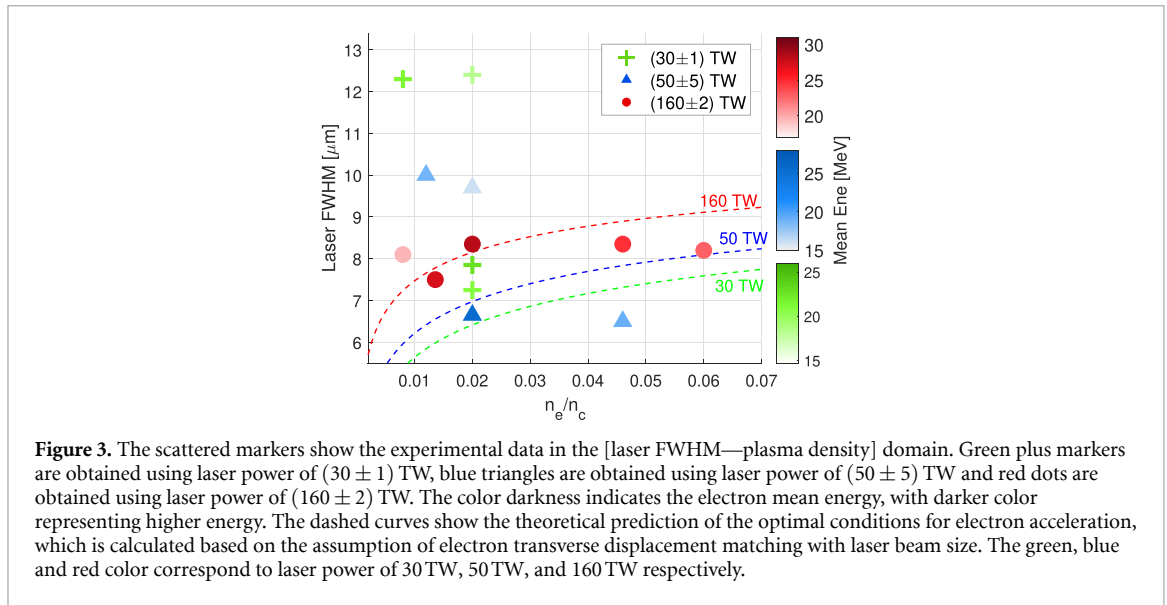
3. PIC modeling

To model the interaction, 2D PIC simulations were performed using the OSIRIS 4.0 code. A $[750\,\mu\mathrm{m} \times 200\,\mu\mathrm{m}]$ moving window with a resolution of 50 cells per λ in longitudinal (x) direction and 35 cells per λ in transverse (y) direction moving in the speed of light was utilized. Each cell has 4 macroparticle electrons and 4 macroparticles representing fully ionized mobile helium ions. An open boundary condition was applied to both dimensions. To approximate the density distribution of a gas jet nozzle, the initial plasma density has a super-Gaussian profile in the x-direction, with a $450\,\mu$m flat top area and two $150\,\mu$m ramping zones connecting to the vacuum as shown in figure 1(b), and a uniform distribution in the y-direction. The maximum plasma density n_0 along the laser propagation axis was $0.01\,n_c$, where $n_c = m_e\epsilon_0\omega_0^2/e^2$ is the critical plasma density and ω_0 is the laser frequency. The laser pulse was linearly polarized in y-direction with $a_0 = 3.5$, a wavelength of 1.053 nm and a pulse duration of $\tau = 700$ fs. It was launched from the vacuum region and focused at $n_e = 0.95n_0$. The initial laser electric field has a Gaussian spatial profile and a temporal form of $E = E_0 \sin(\pi t/\tau)$, where τ is the pulse duration. Three different focal spot sizes with FWHM $= 5\,\mu$m, $8\,\mu$m, and $16\,\mu$m were examined. And since the energy is changing for different focusing conditions, another set of simulations using a constant laser energy of 8.3 J, which is set based on the energy of the $8\,\mu$m beam ($a_0 = 3.5$), were also performed.

Figure 1. (a) Experimental setup. The table on the right shows f-number for four different apodizers and the corresponding in-vacuum laser FWHM. (b) The longitudinal density profile in simulations. n_0 is the peak plasma density, which is 0.02 n_c.

Figure 2. Experimental electron spectra for different laser focal spot sizes with similar peak plasma density of (0.016 ± 0.004) n_c. The light blue curve, labeled as 4.7 μm (2), is a repeat shot of the dark blue shot. The light purple curve, labeled as 8.4 μm (2), is a repeat shot of the dark purple shot. The laser in-vacuum focal spot size, f-number of the apodizer, and the laser power are shown in the legend. The laser a_0 varies for different laser focusing conditions. From small beam size to large beam size, the laser $a_0 = 26$ (FWHM = 4.7 μm), 7.8 (FWHM = 6.7 μm), 9 (FWHM = 8.3 μm), 10.3 (FWHM = 8.4 μm) and 5.7 (FWHM = 10 μm).
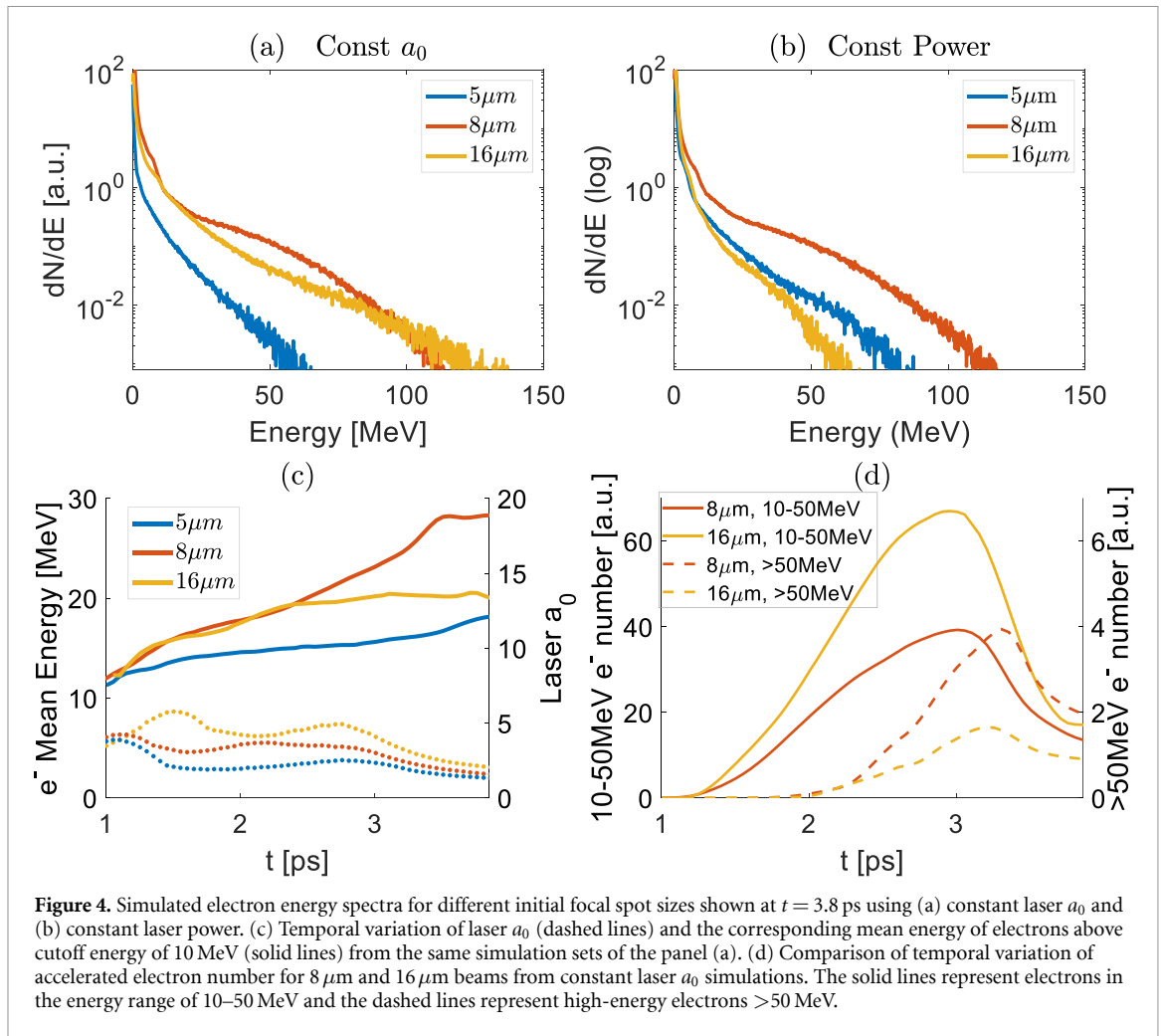
4. Results

The highest electron energy and highest mean energy under the experimental conditions were achieved using a beam with moderate focal spot size. Figure 2 shows seven example experimental electron energy spectra from different laser focal spot sizes at a plasma density of (0.016 ± 0.004) n_c. The apodization of the beam to create the different focal spot sizes means the pulse energy was restricted for the large focal spot sizes, resulting in a wide range of $a_0 = 5.7$–26 for data shown in figure 2. For a laser focal spot of FWHM = 8.3 μm, a bi-Maxwellian-like electron energy distribution extending to ~400 MeV was observed, which exceeds 120 times the ponderomotive energy $U_p = m_e c^2 (\gamma - 1)$, where $\gamma = \sqrt{1 + a_0^2/2}$. Spectra with high energy tails exceeding 50 MeV are obtained for laser focal spot size within the range of 6.7 μm–10 μm. The significant energy increase upon using a moderate-sized beam suggests there is an optimal laser focusing condition. Due to constraints in experimental time, only two shots—one with a laser beam size of 4.7 μm (dark blue curve in figure 2) and another with 8.4 μm (bright red curve in figure 2)—were repeated to check the reproducibility. Both repeated shots show relatively small shot-to-shot variations, particularly for the majority of the electrons below 100 MeV. The 4.7 μm shot and its repeat shot almost overlap, with mean electron energies of 16.6 MeV and 16.8 MeV, respectively. The repeat of the 8.4 μm shot (dashed line) shows a slightly larger gap and has a lower maximum detected energy. The mean energies for the 8.4 μm shot and its repeat shot are 28 MeV and 23 MeV respectively.

Figure 3. The scattered markers show the experimental data in the [laser FWHM—plasma density] domain. Green plus markers are obtained using laser power of (30 ± 1) TW, blue triangles are obtained using laser power of (50 ± 5) TW and red dots are obtained using laser power of (160 ± 2) TW. The color darkness indicates the electron mean energy, with darker color representing higher energy. The dashed curves show the theoretical prediction of the optimal conditions for electron acceleration, which is calculated based on the assumption of electron transverse displacement matching with laser beam size. The green, blue and red color correspond to laser power of 30 TW, 50 TW, and 160 TW respectively.

A wider range of parameter space—density, focal spot size, laser power—was examined in experiments and more data were collected to better extract the energy variation trends. A summary of the results is shown using scattered markers in figure 3. The data is divided into similar laser power, illustrated by the different colors—(30 ± 1) TW (green), (50 ± 5) TW (blue) and (160 ± 2) TW (red)—and the darkness of the color indicates the mean electron energy. The mean electron energy was calculated for electrons above 10 MeV. However, due to the fact that changing the laser focal spot will inevitably change other parameters, such as laser intensity for a fixed laser energy or power, it is difficult to directly separate the individual effects of the laser focusing geometry. Therefore, to understand the complex relationship between the laser focusing geometry and the electron acceleration, we perform two sets of 2D PIC simulations: one with constant laser power and another with constant peak intensity. This allows us to explicitly analyze the electron collective behavior and single particle dynamics. In simulations, the final spectra of escaping electrons are diagnosed outside of the plasma, as the laser entirely leaves plasma at $t = 3.8$ ps. The results of simulations using a constant $a_0 = 3.5$ (corresponding to power of 5 TW, 12 TW, 47 TW for laser FWHM $= 5 \mu$m, 8μm, and 16μm) or constant laser power of 12 TW (corresponding to a_0 of 5.6, 3.5, 2 for laser FWHM $= 5 \mu$m, 8μm, and 16μm) are shown in figures 4(a) and (b) respectively. Enhanced acceleration is obtained using an 8μm beam in both cases and the improvement of electron number is more dramatic in figure 4(b). In addition, due to a low peak laser intensity, the mean electron energy of a 16μm beam is lower than that of a 5μm beam in the constant power simulation. However, due to the simulation having a reduced plasma length scale and less optimal acceleration conditions compared to the best shot in the experiment, the simulated spectra show lower maximum electron energy compared to experimental data.

The 2D simulations provide insight into the influence of laser focusing on the laser field evolution, which is directly related to the channel formation and electron energy gain threshold. Figure 4(c) shows the temporal evolution of the laser a_0 (dashed lines) and the corresponding electron mean energy (solid lines) for three focusing geometries. The center of the laser pulse arrives at the initialized vacuum focal plane of $x = 800 \mu$m at $t = 1.1$ ps. Then it propagates in the peak density region until $t = 3$ ps, and finally the entire laser leaves the plasma at $t = 3.8$ ps. In the density up-ramp region, a beam initially with the smallest spot size reaches peak intensity faster than a large beam. As shown in figure 4(c), the peak a_0 for a 5μm beam appears around 1.1 ps, corresponding to 10μm before the vacuum focus position in the spatial domain, while a 16μm beam reaches its peak intensity at $t = 1.5$ ps, which is roughly 100μm after the vacuum focus point. The 5μm beam reaches its maximum a_0 prior to the vacuum focal plane and the small focal spot has a high transverse ponderomotive force resulting in a narrow, highly cavitated channel. Hence fewer electrons are available within the channel to be accelerated, leading to weaker currents and consequently weak self-generated magnetic fields, as shown in figure 5(a).

After passing the focal plane, a small beam also rapidly defocuses and the a_0 is relatively low for the remaining interaction period. The low laser intensity limits the maximum energy that electrons could gain. In contrast to the tight focusing geometry, we see a more stable a_0 for an 8μm beam. After passing the vacuum focal plane, the laser defocuses to $a_0 = 3$ at $t = 1.6$ ps, then self-focuses to $a_0 = 3.5$ at $t = 1.8$ ps. The a_0 is sustained until it moves to the density down-ramp area. This allows the electron mean energy to increase with a relatively constant slope.

Figure 4. Simulated electron energy spectra for different initial focal spot sizes shown at $t = 3.8$ ps using (a) constant laser a_0 and (b) constant laser power. (c) Temporal variation of laser a_0 (dashed lines) and the corresponding mean energy of electrons above cutoff energy of 10 MeV (solid lines) from the same simulation sets of the panel (a). (d) Comparison of temporal variation of accelerated electron number for 8 μm and 16 μm beams from constant laser a_0 simulations. The solid lines represent electrons in the energy range of 10–50 MeV and the dashed lines represent high-energy electrons >50 MeV.

As the beam diameter increased to 16 μm (corresponding to a higher power), the pulse focuses to highest $a_0 = 6$ at $t = 1.5$ ps. The laser intensity is better sustained along the entire interaction length compared to the smaller beams, with relatively large intensity fluctuations (yellow dotted curve in figure 4(c)). However, as shown in figure 4(c), the mean electron energy curve generated by the 16 μm beam (yellow solid curve) does not surpass that of the 8 μm beam (red solid curve), indicating that the enhanced laser intensity does not improve the mean electron energy. The temporal variation of the accelerated electron number is shown in figure 4(d), for both electrons in the 10–50 MeV and >50 MeV ranges. Before the laser reaches the density down-ramp region (at $t = 3$ ps), the 16 μm beam drives almost twice the number of low-energy (10–50 MeV) electrons compared to the 8 μm beam. However, fewer electrons are able to gain energy above 50 MeV for the 16 μm beam. From 3 ps to 3.5 ps, a large number of electrons lose energy and gradually trail behind the laser. A sheath field is formed at the density down-ramp and channel exit due to the charge separation as the electron beam moves out from plasma to vacuum. This causes the reduction in electron number, particularly for the lower energy electrons which could lose all the energy before exiting the sheath field, leading to a lower final mean electron energy.

The focusing geometry also implies laser longitudinal fields. Previous research has demonstrated that the transverse E_y field does positive work for DLA electrons, whereas the longitudinal E_x laser field tends to decelerate electrons [14]. The ratio of laser transverse and longitudinal electric field is observed to be higher for the larger focal spots ($|E_y|/|E_x|_{5\,\mu m} : |E_y|/|E_x|_{8\,\mu m} = 19:26$ at 2.2 ps). Therefore, compared to the smallest focal spot, the longitudinal electric field of larger focal spots is expected to do relatively less negative work.

To investigate the effect of the longitudinal laser field and sheath field for each case, the energy contributions from different field components are calculated by performing particle tracking. Seven hundred macro particles were randomly selected from electrons that move along with the laser and eventually out of the plasma. They were tracked from the start of the simulations to the time when the laser completely exits the plasma. The positions, momentum, and the exerted electric fields of the tagged electrons were diagnosed at every time interval of 25 fs. The work done by longitudinal electric field E_x and transverse electric field E_y
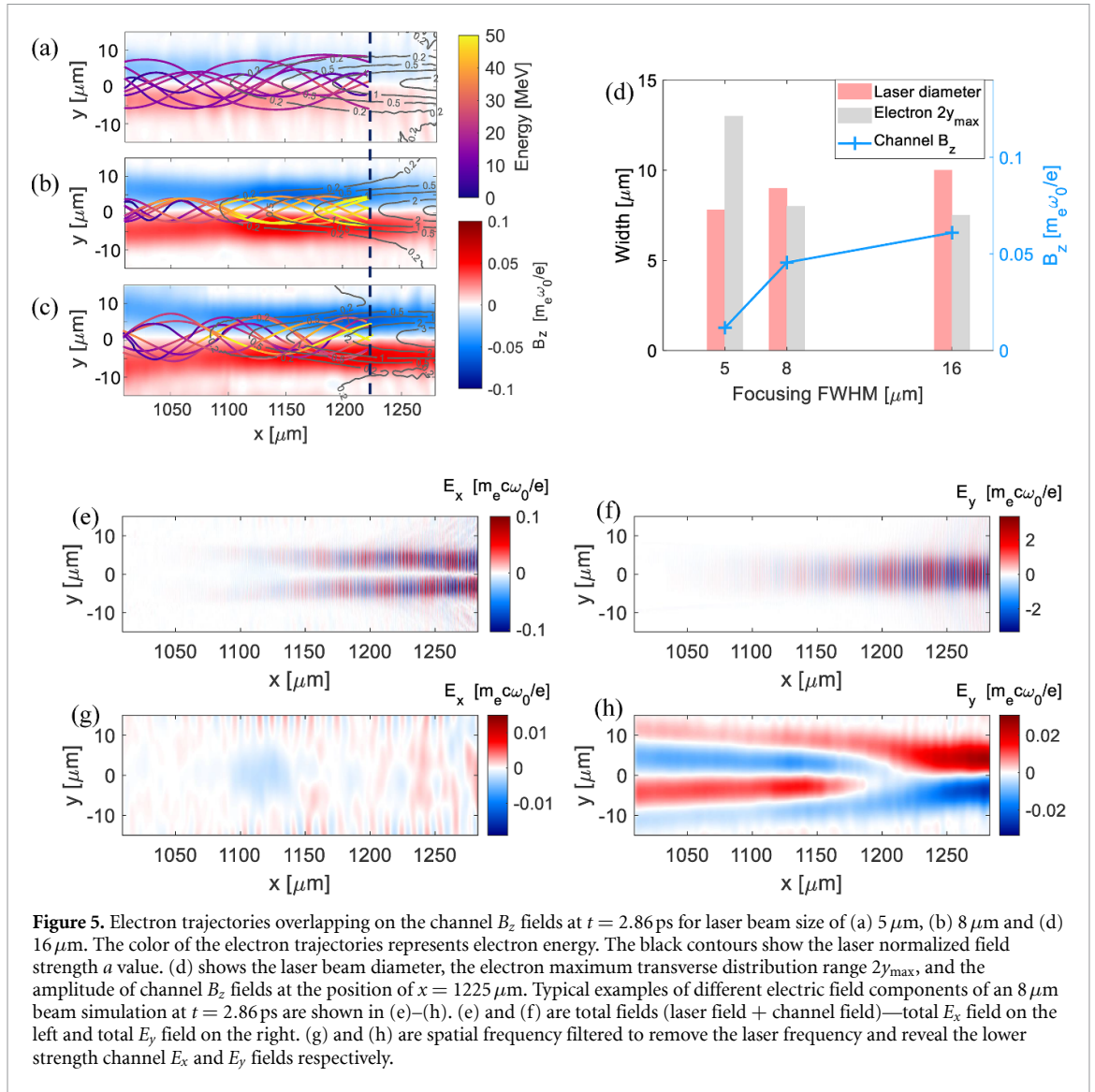
Figure 5. Electron trajectories overlapping on the channel B_z fields at $t = 2.86$ ps for laser beam size of (a) $5\,\mu$m, (b) $8\,\mu$m and (d) $16\,\mu$m. The color of the electron trajectories represents electron energy. The black contours show the laser normalized field strength a value. (d) shows the laser beam diameter, the electron maximum transverse distribution range $2y_{max}$, and the amplitude of channel B_z fields at the position of $x = 1225\,\mu$m. Typical examples of different electric field components of an $8\,\mu$m beam simulation at $t = 2.86$ ps are shown in (e)–(h). (e) and (f) are total fields (laser field + channel field)—total E_x field on the left and total E_y field on the right. (g) and (h) are spatial frequency filtered to remove the laser frequency and reveal the lower strength channel E_x and E_y fields respectively.

are calculated by time integrals of $W_{E_x} = -\int_0^t |e|E_x \cdot v_x \, dt'$ and $W_{E_y} = -\int_0^t |e|E_y \cdot v_y \, dt'$, where v_x and v_y are electron longitudinal and transverse velocities respectively [4].

Figure 6 shows the distribution of the tracked electrons in the $[W_{E_x}, W_{E_y}]$ energy space before ($t = 3.3$ ps, orange markers) and after ($t = 4$ ps, blue markers) the sheath field region for the three focusing geometries. The vast majority of the electrons are located in the quadrant of $W_{E_y} > 0$ and $W_{E_x} < 0$, where electrons gain energy from the transverse laser electric fields and lose energy due to longitudinal electric fields, providing explicit evidence of DLA mechanism [4]. The electrons generated by a $5\,\mu$m focal spot are more tilted towards W_{E_x} axis in figure 6(a), indicating a greater proportion of negative work was done by the longitudinal laser electric field. Also, the blue markers almost overlap with the orange ones, implying that the electron distribution is minimally affected by the sheath field. For the moderate and large beams, the majority of pre-sheath field (orange) electrons are scattered around a direction of $W_{E_y}/W_{E_x} \sim 3/1$ at $t = 3.3$ ps, corresponding to the time of the high-energy electron number reaches peaks in figure 4(d). However, the difference is that fewer orange electrons exceed 50 MeV for a $16\,\mu$m beam as shown in figure 6(c), as previously discussed. Secondly, a larger number of electrons are driven out of plasma by a large focal spot (higher power pulse), hence a stronger sheath field grows in the down-ramp of the plasma, resulting in a greater impact on electron distribution. The blue markers shift leftward along the negative W_{E_x} direction and there is a wider gap between orange and blue electrons for the largest focal spot, suggesting more energy loss in the sheath field and a lower final energy compared to the mid-sized beam.

The particle tracking also reveals more details of the individual electron temporal and spatial dynamics. Figure 5 depicts the trajectories of eight typical energetic electrons overlaid on the instantaneous channel azimuthal magnetic fields B_z (figures 5(a)–(c)) at the time of electrons arriving at $x = 1222\,\mu$m for different laser focusing conditions. And the black contours outline the laser normalized field strength a. Figure 5(b)
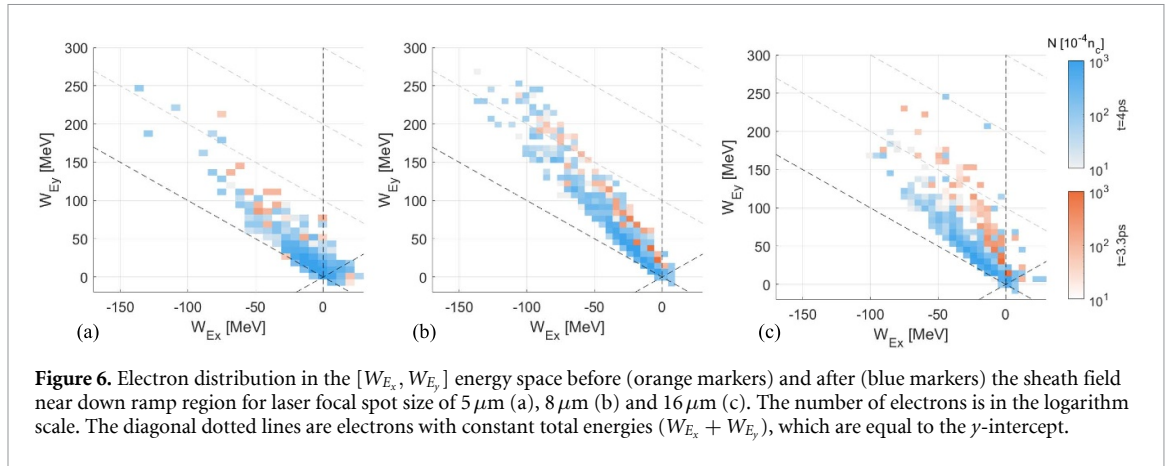
Figure 6. Electron distribution in the $[W_{E_x}, W_{E_y}]$ energy space before (orange markers) and after (blue markers) the sheath field near down ramp region for laser focal spot size of $5\,\mu$m (a), $8\,\mu$m (b) and $16\,\mu$m (c). The number of electrons is in the logarithm scale. The diagonal dotted lines are electrons with constant total energies ($W_{E_x} + W_{E_y}$), which are equal to the y-intercept.

clearly shows that electrons gain much higher energy with a moderate-sized driving pulse. To better illustrate the relative scale of electron oscillation to the area that the laser field extends transversely, the maximum electron transverse position ($2y_{\max}$) and laser beam diameter ($2r$) at $x = 1222\,\mu$m are presented using gray and red histograms in figure 5(d). The peak channel B_z field amplitude is also plotted in figure 5(d). As the channel expands with increased laser focal spot size, more electrons may be accommodated within the laser field and accelerated. As a consequence, stronger currents flow in the channel, forming a stronger B_z field. This self-generated quasi-static magnetic field assists the acceleration process by confining the electron radial excursion and deflecting the electrons in the forward direction [24]. Therefore, electrons are confined more tightly within the wider channel because of the stronger magnetic field, as shown by the gray histogram gradually becoming shorter than the red in figure 5(d). The ratio $r/y_{\max}$ is 0.6, 1.1, and 1.4 for laser focal FWHM of $5\,\mu$m, $8\,\mu$m and $16\,\mu$m respectively. Therefore, for a $5\,\mu$m beam, the magnetic field is too weak to confine the electron in a way to efficiently allow DLA at $y_{\max}$; for an $8\,\mu$m beam, the electron transverse displacement is well-matched to the laser beam width; while for a $16\,\mu$m beam, electrons are over-confined to a column narrower than the laser size.

Additionally, the longitudinal and transverse components of electric fields of an $8\,\mu$m beam are shown in figures 5(e)–(h), with (e) and (f) showing the total fields that are dominated by the laser fields. Spatially filtering out the laser frequency reveals the lower strength channel fields in figures 5(g) and (h). The channel E_y field (figure 5(h)) is undergoing a field reversal at this time due to the motion of the ions [25]. Therefore, the azimuthal magnetic field is dominant in confining the electron beam within the channel.

Given that the maximum electron oscillation matches the laser beam size in the optimal scenario, a theoretical model can be developed to predict the optimal focusing geometry to a broader range of laboratory conditions. In the laser channel, quasi-static electric and magnetic fields are generated and the laser beam size is approximately equal to the channel width. Assuming that the ponderomotive force is balanced by the force of the charge separation in a stable ion channel, the channel width (w) can be estimated as approximately twice the laser spot radius (r) [26, 27], so that $w \approx 2r = 2 \cdot 2\sqrt{a_0'} \cdot c/\omega_p$, where a_0' is the normalized laser field strength when the laser is in the channel and ω_p is the plasma frequency. Since the laser power $P_L \propto a_0'^2 r^2 \sim a_0^2 r_0^2$, the laser spot size can be rewritten as

$$r = w/2 = \left[\left(2c/\omega_p\right)^2 \cdot a_0 r_0\right]^{1/3}, \tag{1}$$

where r_0 is the laser spot radius at the focal plane. In [18, 28], the maximum resonant electron transverse excursion from the channel axis is calculated using

$$y_{\max} = \left(2c/\omega_p\right)\sqrt{\left(\frac{a_0}{\epsilon} \cdot \frac{\omega_p}{\omega_0}\right)^{2/3} - 1}, \tag{2}$$

where ϵ is a parameter depending on the initial conditions. Here we take $\epsilon = 0.2$ for an ideal acceleration condition [18]. Equating equations (1) and (2),

$$\left(a_0 r_0\right)^{1/3} = \left(2c/\omega_p\right)^{1/3}\sqrt{\left(\frac{a_0}{\epsilon} \cdot \frac{\omega_p}{\omega_0}\right)^{2/3} - 1}$$

gives a condition where the electron transverse oscillation amplitude matches the laser spot size.

The results are plotted in figure 3 using dashed curves with green, blue, and red color showing laser power of 30 TW, 50 TW and 160 TW respectively. For each certain curve, the laser power is constant. Each position on this curve gives the optimal laser focusing FWHM for different plasma densities to reach maximum electron energy according to the simple model. Take the red curve for example, it has a fixed laser power of 160 TW, and the optimal laser FWHM for a plasma density of $n_e = 0.02\, n_c$ is 8.2 μm. For each laser power, the optimal laser focal spot size increases with the plasma density.

To examine the validity of the simple theoretic model, the experimental data are plotted using scattered markers in the [Laser FWHM—n_e] space in figure 3. The darkest red and blue markers, representing the highest mean energies measured, are located quite close to the red and blue dashed curves respectively. This indicates that the optimized experimental parameter sets (laser power, laser focusing, and plasma density), which produced the electron beam with maximum mean energy, agree with the theoretical prediction of the ideal acceleration conditions. For the low laser power of 30 TW, there is not enough experimental data showing a clear energy variation trend. Therefore, at least for laser power above 30 TW, the theoretical calculation based on the assumption of electron oscillation matching with the laser beam size provides a good prediction of the optimal combination of laser and plasma parameters.

5. Summary

In conclusion, this work has experimentally demonstrated that optimizing the laser focusing geometry significantly enhances electron energy gain via DLA, and a maximum energy of $\sim$400 MeV was observed using a hundred TW laser in experiments. To focus the laser energy on the smallest possible focal spot to achieve the highest intensity is not always advantageous for DLA. The optimal focusing geometry is achieved when the electron transverse oscillation amplitude matches the laser spot size in plasma, which is roughly the channel width. And based on the matching condition, a model is developed to find the optimal combination of laser power, focusing condition and plasma density in experiments. Electrons from an optimal focal spot gain more energy than a tightly focused beam in bulk plasma and lose less energy than a very large beam in rarefied plasma and sheath field. This demonstration and optimization of high-energy electron beams paves the way towards high-fluence x-ray beams delivered on a picosecond time scale [29], which promise to enhance the radiographic capabilities of moderate relativistic intensity laser systems operating in high-energy-density research. For example, the picosecond duration of the x-ray beam generated by DLA electrons are particularly suitable for radiography applications on longer timescales. Phenomena that evolve on nanosecond timescales like shock waves propagating through dense plasma require high photon flux to freeze the dynamics in a single shot [29, 30]. Furthermore, an x-ray beam with high energy and brightness is ideal for imaging high density objects [31]. Simulations performed by Rosmej *et al* have demonstrated the feasibility of performing x-ray phase contrast imaging of a sphere using DLA x-ray which has a photon number of 7×10^{11} in the 1–30 keV range, brilliance of $\geqslant 6 \times 10^{19}$ photons s^{-1} mm^{-2} mrad^{-2} $(0.1\%$ BW$)^{-1}$ at a critical energy of 5 keV [29]. Moreover, investigations into channel formation and field evolution are relevant to the hole boring scheme for fast ignition inertial confinement fusion [32]. In this scheme, a high energy laser pulse needs to propagate through a millimeter-scale underdense plasma before reaching overdense plasma and the dense fuel. One of the key concerns is the energy transport from the laser into the fast electrons—in fact here a high conversion efficiency into the $\sim$1 MeV electrons is the goal—and the formation of channel fields could play an important role in guiding laser pulse and collimating ignition electrons [33–36].
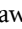
Data availability statement

All data that support the findings of this study are included within the article (and any supplementary files).

Acknowledgments

ORCID iDs

H Tang ⓘ https://orcid.org/0000-0003-4885-6863
R Babjak ⓘ https://orcid.org/0000-0002-2174-4987
I-L Yeh ⓘ https://orcid.org/0000-0003-0796-717X
P T Campbell ⓘ https://orcid.org/0000-0002-7192-0221
Y Ma ⓘ https://orcid.org/0000-0002-3919-4856
B K Russell ⓘ https://orcid.org/0000-0003-0011-2419
J L Shaw ⓘ https://orcid.org/0000-0002-1118-8921
A G R Thomas ⓘ https://orcid.org/0000-0003-3206-8512
A V Arefiev ⓘ https://orcid.org/0000-0002-0597-0976
L Willingale ⓘ https://orcid.org/0000-0003-4304-0339

References

[1] Strickland D and Mourou G 1985 Compression of amplified chirped optical pulses *Opt. Commun.* **55** 447–9
[2] Mourou G A, Barty C P and Perry M D 1997 Ultrahigh-intensity laser: physics of the extreme on a tabletop (https://doi.org/10.1063/1.882131)
[3] Pukhov A, Sheng Z-M and Meyer-ter Vehn J 1999 Particle acceleration in relativistic laser channels *Phys. Plasmas* **6** 2847–54
[4] Gahn C, Tsakiris G D, Pukhov A, Meyer-ter Vehn J, Pretzler G, Thirolf P, Habs D and Witte K J 1999 Multi-MeV electron beam generation by direct laser acceleration in high-density plasma channels *Phys. Rev. Lett.* **83** 4772
[5] Meyer-ter Vehn J and Sheng Z M 1999 On electron acceleration by intense laser pulses in the presence of a stochastic field *Phys. Plasmas* **6** 641–4
[6] Willingale L *et al* 2006 Collimated multi-MeV ion beams from high-intensity laser interactions with underdense plasma *Phys. Rev. Lett.* **96** 245002
[7] Pomerantz I *et al* 2014 Ultrashort pulsed neutron source *Phys. Rev. Lett.* **113** 184801
[8] Vranic M, Klimo O, Korn G and Weber S 2018 Multi-GeV electron-positron beam generation from laser-electron scattering *Sci. Rep.* **8** 1–11
[9] Martinez B, Barbosa B and Vranic M 2023 Creation and direct laser acceleration of positrons in a single stage *Phys. Rev. Accel. Beams* **26** 011301
[10] Kneip S *et al* 2008 Observation of synchrotron radiation from electrons accelerated in a petawatt-laser-generated plasma cavity *Phys. Rev. Lett.* **100** 105006
[11] Grazia Ronga M, Cavallone M, Patriarca A, Maia Leite A, Loap P, Favaudon V, Créhange G and De Marzi L 2021 Back to the future: very high-energy electrons (VHEEs) and their potential application in radiation therapy *Cancers* **13** 4942
[12] Morimoto Y and Baum P 2018 Diffraction and microscopy with attosecond electron pulse trains *Nat. Phys.* **14** 252–6
[13] Bin J H *et al* 2018 Enhanced laser-driven ion acceleration by superponderomotive electrons generated from near-critical-density plasma *Phys. Rev. Lett.* **120** 074801
[14] Arefiev A V, Khudik V N, Robinson A P L, Shvets G, Willingale L and Schollmeier M 2016 Beyond the ponderomotive limit: direct laser acceleration of relativistic electrons in sub-critical plasmas *Phys. Plasmas.* **23** 056704
[15] Hussein A E *et al* 2021 Towards the optimisation of direct laser acceleration *New J. Phys.* **23** 023031
[16] Willingale L *et al* 2018 The unexpected role of evolving longitudinal electric fields in generating energetic electrons in relativistically transparent plasmas *New J. Phys.* **20** 093024
[17] Tangtartharakul K, Yeh I, Tang H, Wang T, Willingale L and Arefiev A 2022 Mitigation of the detrimental role of the longitudinal laser electric field during direct laser acceleration of electrons *APS Division of Plasma Physics Meeting Abstracts* JP11–026
[18] Babjak R, Willingale L, Arefiev A and Vranic M 2024 Direct laser acceleration in underdense plasmas with multi-PW lasers: a path to high-charge, GeV-class electron bunches *Phys. Rev. Lett.* **132** 125001
[19] Thomas A G R *et al* 2007 Effect of laser-focusing conditions on propagation and monoenergetic electron production in laser-wakefield accelerators *Phys. Rev. Lett.* **98** 095004
[20] Fonseca R A *et al* 2002 OSIRIS: a three-dimensional, fully relativistic particle in cell code for modeling plasma based accelerators *Int. Conf. on Computational Science* (Springer) pp 342–51
[21] Hemker R G 2000 Particle in cell modeling of plasma based accelerators in two-dimensions and three-dimensions *Thesis* University of California, Los Angeles
[22] Chen H, Link A J, Van Maren R, Patel P K, Shepherd R, Wilks S C and Beiersdorfer P 2008 High performance compact magnetic spectrometers for energetic ion and electron measurement in ultraintense short pulse laser solid interactions *Rev. Sci. Instrum.* **79** 10E533
[23] von der Linden J, Ramos-Méndez J, Faddegon B, Massin D, Fiksel G, Holder J P, Willingale L, Peebles J, Edwards M R and Chen H 2021 Dispersion calibration for the national ignition facility electron–positron–proton spectrometers for intense laser matter interactions *Rev. Sci. Instrum.* **92** 033516
[24] Gong Z, Mackenroth F, Wang T, Yan X Q, Toncian T and Arefiev A V 2020 Direct laser acceleration of electrons assisted by strong laser-driven azimuthal plasma magnetic fields *Phys. Rev. E* **102** 013206
[25] Kar S *et al* 2007 Dynamics of charge-displacement channeling in intense laser–plasma interactions *New J. Phys.* **9** 402
[26] Davis J, Petrov G M and Velikovich A L 2005 Dynamics of intense laser channel formation in an underdense plasma *Phys. Plasmas* **12** 123102

[27] Lu W, Tzoufras M, Joshi C, Tsung F S, Mori W B, Vieira J, Fonseca R A and Silva L O 2007 Generating multi-GeV electron bunches using single stage laser wakefield acceleration in a 3D nonlinear regime *Phys. Rev. Spec. Top. Accel. Beams* **10** 061301

[28] Arefiev A V, Khudik V N and Schollmeier M 2014 Enhancement of laser-driven electron acceleration in an ion channel *Phys. Plasmas* **21** 033104

[29] Rosmej O N *et al* 2021 Bright betatron radiation from direct-laser-accelerated electrons at moderate relativistic laser intensity *Matter Radiat. Extremes* **6** 048401

[30] Barbato F *et al* 2019 Quantitative phase contrast imaging of a shock-wave with a laser-plasma based x-ray source *Sci. Rep.* **9** 18805

[31] Rusby D R *et al* 2016 Pulsed x-ray imaging of high-density objects using a ten picosecond high-intensity laser driver *Proc. SPIE* **9992** 61–68

[32] Tabak M, Hammer J, Glinsky M E, Kruer W L, Wilks S C, Woodworth J, Campbell E M, Perry M D and Mason R J 1994 Ignition and high gain with ultrapowerful lasers *Phys. Plasmas* **1** 1626–34

[33] Li G, Yan R, Ren C, Wang T-L, Tonge J and Mori W B 2008 Laser channeling in millimeter-scale underdense plasmas of fast-ignition targets *Phys. Rev. Lett.* **100** 125002

[34] Lei A L *et al* 2007 Relativistic laser channeling in plasmas for fast ignition *Phys. Rev. E* **76** 066403

[35] Willingale L *et al* 2011 High-power, kilojoule class laser channeling in millimeter-scale underdense plasma *Phys. Rev. Lett.* **106** 105002

[36] Scott R H H *et al* 2012 A study of fast electron energy transport in relativistically intense laser-plasma interactions with large density scalelengths *Phys. Plasmas* **19** 053104